

Geometrical transport in pseudospin-1 fermions

Adesh Singh  and Gargee Sharma *School of Physical Sciences, Indian Institute of Technology Mandi, Mandi 175005, India*

(Received 12 December 2022; revised 10 May 2023; accepted 23 June 2023; published 30 June 2023)

Electronic transport in the $\alpha\mathcal{T}_3$ model of pseudospin-1 fermions with a finite gap is studied within the semiclassical Boltzmann approximation. We show that coupling of the orbital magnetic moment to the external magnetic field, which is otherwise absent in the massless model, breaks valley symmetry, results in finite and measurable corrections to the longitudinal and Hall conductivity, and yields a geometrical contribution to the Hall conductivity due to the Berry curvature. We also show that, for a generic two-dimensional system, remarkably, magnetoresistance induced by the orbital magnetic moment can be either positive or negative; the sign depends on the amount of disorder and is different for both conventional and geometric contributions to the magnetoresistance.

DOI: [10.1103/PhysRevB.107.245150](https://doi.org/10.1103/PhysRevB.107.245150)

I. INTRODUCTION

The importance of Berry's phase and Berry curvature effects in solids is now very well established [1–5]. While Berry curvature in solids leads to anomalous Hall effects [6], more recently, it has been realized that it can also explain exotic effects, such as the chiral anomaly in Weyl semimetals, within the semiclassical Boltzmann approximation [7]. While Berry curvature has received significant attention, the role of the anomalous orbital magnetic moment has been explored far less. Cognate to the Berry curvature, the orbital magnetic moment also owes its origin to the geometrical effects in the Bloch bands [4]. Specifically, the self-rotating angular momentum of the Bloch wave packet gives rise to an anomalous orbital magnetic moment that couples to the external magnetic field via a Zeeman-like interaction. This phenomenon has recently yielded unconventional effects in semiclassical electronic transport [8–13].

In recent times, graphene and similar other Dirac materials have received the attention of diverse audiences due to their unconventional energy dispersion and nontrivial topology of their Bloch wave functions [14–16]. On the other hand, the interest in dispersionless flat bands has been rejuvenated after the discovery of superconductivity in twisted bilayer graphene [17]. First proposed in Ref. [18], the $\alpha\mathcal{T}_3$ model synthesizes flat and dispersive Dirac bands in a single model. The tight-binding description of the $\alpha\mathcal{T}_3$ model comprises a hexagonal lattice with atoms situated at the vertices of the hexagons and their centers. Thus the unit cell consists of three atoms, constructing the electronic-state description that of a triple-component fermion (pseudospin-1 fermions). Varying the parameter α in the $\alpha\mathcal{T}_3$ lattice, one interpolates between graphene ($\alpha = 0$) and the dice lattice ($\alpha = 1$). When $\alpha \in (0, 1]$, the band structure is remarkably independent of α consisting of a flat band at zero energy intersecting a Dirac cone. Experimentally, in solid state physics, the $\alpha\mathcal{T}_3$ model can be realized in trilayers of cubic lattices and $\text{Hg}_{1-x}\text{Cd}_x\text{Te}$ quantum wells [19–21].

While the $\alpha\mathcal{T}_3$ spectrum is gapped in an external magnetic field, the flat band remains primarily unaffected [18]. Some

other recent works have discussed the stability of the flat bands to impurities, the presence of boundaries, and perturbative radiation [22–24]. In the $\alpha\mathcal{T}_3$ model, while the Dirac cone may gap out due to these factors, simply shifting the chemical potential in one or more of the sublattices can also produce a Dirac gap (massive pseudospin-1 fermions). The massless $\alpha\mathcal{T}_3$ model's optical, magnetic, and electronic transport properties have been studied [22,25–32]; investigations on the gapped model remain less explored. While owing certain similarities to the physics of pseudospin-1/2 fermions in massive graphene models [10,33], as we show later, the presence of a dispersionless (or weakly dispersive) flat band in pseudospin-1 fermions strikingly changes the topology of the wave functions, and, more so, the geometrical quantities such as the Berry curvature and the orbital magnetic moment. The variation of these quantities with the lattice parameters α is insightful as well and reflects the $\alpha \rightarrow 1/\alpha$ duality.

Here we study the electronic transport properties of the massive $\alpha\mathcal{T}_3$ model, focusing particularly on the nontrivial role of the anomalous orbital magnetic moment. We first discuss the implications of the Dirac gap on conventional transport in the absence and presence of an external magnetic field, specifically evaluating the longitudinal and the Hall conductivity for three different disorder profiles: δ -correlated impurities, Gaussian impurities, and screened Coulomb impurities. A crucial distinction between massless and massive pseudospin-1 fermions is the presence of Berry curvature and orbital magnetic moment. While the Berry curvature and orbital magnetic moment are absent in the massless case, as we show, both acquire finite contributions in the massive model. We show that coupling the orbital magnetic moment to the external magnetic field breaks valley symmetry, results in finite and measurable corrections to the longitudinal and Hall conductivity, and yields a geometrical contribution to the Hall conductivity due to the Berry curvature. Strikingly, the orbital magnetic moment induces a finite magnetoresistance (longitudinal), which can be either positive or negative, different from the claim in Ref. [10] in the context of pseudospin-1/2 fermions. We show that the sign of the magnetoresistance

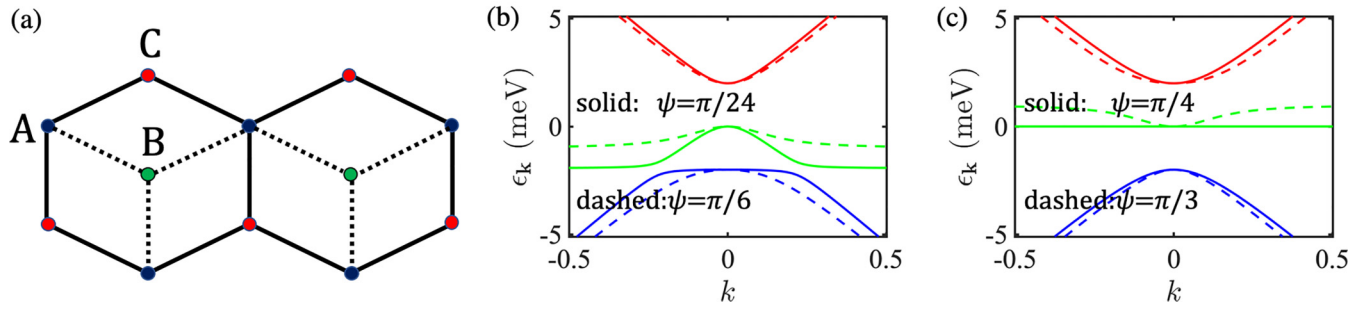


FIG. 1. (a) Lattice structure of the α - T_3 model. (b) Band structure of the massive α - T_3 model for $\psi = \pi/24$ (solid lines) and for $\psi = \pi/6$ (dashed lines). (c) Band structure for $\psi = \pi/4$ (solid lines) and for $\psi = \pi/3$ (dashed lines). The dimensions of k are normalized by $1/a$, where $a = 50$ nm. We choose $m = 2$ meV.

depends on the amount of disorder, switching from positive to negative for the case of conventional contribution to the Hall effect and switching vice versa for geometric contribution to the Hall effect. Introducing a generic model of magnetoresistance, we conjecture that both positive and negative magnetoresistance could be observed in the model considered in Ref. [10]. Our analysis assumes the semiclassical Boltzmann approximation that remains valid for weak external electric and magnetic fields.

II. MASSIVE PSEUDOSPIN-1 FERMIONS

A. Hamiltonian and band structure

The α - T_3 model consists of three sublattices that we name A , B , and C . Sites A and C occupy the positions corresponding to the two sublattices in graphene, while the center of each hexagon has an additional site, B . The hopping parameters among various sites are $t_{AC} = t$ and $t_{BC} = \alpha t$. As the parameter α varies from zero to one, the lattice structure interpolates from graphene to a dice lattice. Figure 1(a) plots the representative real-space lattice structure. Here, we consider the α - T_3 model with an additional mass term m , such that the momentum-space Hamiltonian near the \mathbf{K} point is expressed as $H_{\mathbf{k}}^{\tau} = H_0^{\tau} + H_m$, where [34–36]

$$H_0^{\tau} = \tau \hbar v k \begin{pmatrix} 0 & \cos \psi e^{-i\tau\phi} & 0 \\ \cos \psi e^{i\tau\phi} & 0 & \sin \psi e^{-i\tau\phi} \\ 0 & \sin \psi e^{i\tau\phi} & 0 \end{pmatrix},$$

$$H_m = m \begin{pmatrix} 1 & 0 & 0 \\ 0 & 0 & 0 \\ 0 & 0 & -1 \end{pmatrix}. \quad (1)$$

Here $\tau = \pm 1$ stands for the valley index, v is the velocity parameter, $\tan \psi = \alpha$, $\tan \phi = k_y/k_x$, and m is assumed to have the dimensions of energy. When $m = 0$, the energy spectrum is independent of α and the eigenvalues are $\epsilon_{\mathbf{k}} = 0$, $+\hbar v_F k$, and $-\hbar v_F k$, corresponding to a flat zero-energy band intersecting the linearly dispersing Dirac cone. It is important to briefly discuss how the massive α - T_3 model may be experimentally realized. While disorder or magnetic field may generate a nonzero mass m , it may also be generated by

shifting the chemical potential on sublattices A and B or by making the atoms nonidentical on the sublattices. For example, appropriately doping trilayers of cubic lattices may result in an effective low-energy model that resembles the massive α - T_3 model. For example, Ref. [37] studies the effect of doping on the transport properties of a cubic lattice structure. In the presence of the mass term, the spectrum is solved by solving the following cubic equation:

$$\epsilon_{\mathbf{k}}^3 - \epsilon_{\mathbf{k}}(m^2 + \hbar^2 v^2 k^2) - m \hbar^2 v^2 k^2 \cos(2\psi) = 0. \quad (2)$$

The above cubic equation may be solved via Cardano's method. The exact analytical expressions for the band dispersions for arbitrary values of m and ψ could be more illuminating, so we do not discuss them here; below, we present their approximate form in some exceptional limiting cases:

$$\epsilon_{\mathbf{k}}(\psi = \pi/4) = \begin{cases} +\sqrt{\hbar^2 v^2 k^2 + m^2}, \\ 0, \\ -\sqrt{\hbar^2 v^2 k^2 + m^2}, \end{cases} \quad (3)$$

$$\epsilon_{\mathbf{k}}(\hbar v k \gg m) = \begin{cases} \tau \hbar v k + m \cos(2\psi)/2 + O(m^2), \\ -m \cos(2\psi) + O(m^2), \\ -\tau \hbar v k + m \cos(2\psi)/2 + O(m^2), \end{cases} \quad (4)$$

$$\epsilon_{\mathbf{k}}(\hbar v k \ll m) = \begin{cases} m + m^{-1} \hbar^2 v^2 k^2 \cos^2 \psi + O(k^3), \\ -m^{-1} \hbar^2 v^2 k^2 \cos(2\psi) + O(k^3), \\ -m - m^{-1} \hbar^2 v^2 k^2 \sin^2 \psi + O(k^3). \end{cases} \quad (5)$$

When $m \neq 0$, the linearly dispersing cone gaps out and the qualitative behavior of the middle band (which is dispersionless for $m = 0$) depends on the value of ψ , roughly scaling as $\sim -\cos(2\psi)$. Therefore, when $\psi < \pi/4$, the middle band hosts a holelike pocket, and when $\psi > \pi/4$, it hosts an electronlike pocket. When $\psi = \pi/4$, the band is nondispersive. When $k \ll m/\hbar v$, the middle and the upper bands are quadratic in k and are linear when $k \gg m/\hbar v$. Figures 1(b) and 1(c) present the band structure for a few different values ψ for a fixed m . Since the band dispersion is isotropic with respect to the polar angle ϕ , we plot the band structure as a function of radial coordinate k .

B. Conventional magnetotransport

We first discuss conventional magnetotransport in pseudospin-1 fermions. To this end, we focus on three specific quantities: Longitudinal conductance (σ_{xx}), conventional Hall conductance (σ_{xy}), and the geometrical Hall conductance (σ_{xy}^a). These are given by the following expressions in the weak-field Boltzmann approximation:

$$\begin{aligned}\sigma_{xx} &= \frac{e^2}{\hbar} \int \frac{d^2k}{(2\pi)^2} \left(\frac{-\partial f_0(\epsilon_{\mathbf{k}})}{\partial \epsilon_{\mathbf{k}}} \right) \tau_{\mathbf{k}} \left(\frac{\partial \epsilon_{\mathbf{k}}}{\hbar \partial k_x} \right)^2, \\ \sigma_{xy} &= \frac{e^3 b}{\hbar} \int \frac{d^2k}{(2\pi)^2} \left(\frac{-\partial f_0(\epsilon_{\mathbf{k}})}{\partial \epsilon_{\mathbf{k}}} \right) \left(\frac{\tau_{\mathbf{k}} \partial \epsilon_{\mathbf{k}}}{\hbar \partial k_y} \right) \\ &\quad \times \left(\frac{\partial \epsilon_{\mathbf{k}}}{\hbar \partial k_y} \frac{\partial}{\partial k_x} - \frac{\partial \epsilon_{\mathbf{k}}}{\hbar \partial k_x} \frac{\partial}{\partial k_y} \right) \left(\frac{\tau_{\mathbf{k}} \partial \epsilon_{\mathbf{k}}}{\hbar \partial k_x} \right), \\ \sigma_{xy}^a &= - \int \frac{d^2k}{(2\pi)^2} \Omega^z(\mathbf{k}) f_0(\epsilon_{\mathbf{k}}).\end{aligned}\quad (6)$$

Here b is the applied magnetic field, $-e$ is the charge of an electron, $f_0(\epsilon_{\mathbf{k}})$ is the Fermi-Dirac distribution function, $\Omega^z(\mathbf{k})$ is the z component of the Berry curvature, and $\tau_{\mathbf{k}}$ is the relaxation time. The relaxation time is evaluated as [38]

$$\frac{1}{\tau_{\mathbf{k}}} = \int \frac{d^2k'}{(2\pi)^2} w_{\mathbf{k},\mathbf{k}'} (1 - \cos \phi_{\mathbf{k}\mathbf{k}'}), \quad (7)$$

where $\cos \phi_{\mathbf{k}\mathbf{k}'}$ is the angle between the vectors \mathbf{k} and \mathbf{k}' and $w_{\mathbf{k},\mathbf{k}'}$ is the scattering amplitude between the states $|\mathbf{k}\rangle$ and $|\mathbf{k}'\rangle$, which strongly depends on the type of impurity scattering considered. Although anisotropy on the Fermi surface invalidates the use of Eq. (7), this is irrelevant here since the band dispersion is isotropic. Here we study the effects of three different types of impurities: (i) δ -correlated impurities, (ii) screened Coulomb impurities, and (iii) Gaussian impurities. The general form of the impurity potential is expressed as a sum of impurity potentials located at sites \mathbf{R}_i :

$$V_{\text{imp}}(\mathbf{r}) = \sum_i u(\mathbf{r} - \mathbf{R}_i), \quad (8)$$

where the function $u(\mathbf{r})$ takes the following form for each of the impurity types:

$$\begin{aligned}u^\delta(\mathbf{r}) &= V_\delta \delta(\mathbf{r}), \\ u^c(\mathbf{r}) &= \frac{e^2 e^{-rk_{\text{TF}}}}{4\pi \epsilon_0 \kappa r}, \\ u^g(\mathbf{r}) &= V_g e^{-r^2/2\sigma^2}.\end{aligned}\quad (9)$$

The superscripts c , δ , and g stand for Coulomb, δ (delta), and Gaussian impurities, respectively. The various parameters used above are explained as follows: (i) for δ disorder, V_δ is the bare impurity strength, (ii) for Coulomb disorder, κ is the dielectric constant and k_{TF} is the Thomas-Fermi screening wave vector, and (iii) for Gaussian disorder, V_g is the bare impurity strength and σ is the standard deviation of the Gaussian function. The scattering rate for each of the impurity types can be evaluated in the lowest Born approximation to

be [38]

$$\begin{aligned}w_{\mathbf{k},\mathbf{k}'}^\delta &= \frac{2\pi}{\hbar} \frac{n_i^\delta}{\mathcal{A}} V_\delta^2 |\langle \mathbf{k}' | \mathbf{k} \rangle|^2 \delta(\epsilon_{\mathbf{k}} - \epsilon_{\mathbf{k}'}), \\ w_{\mathbf{k},\mathbf{k}'}^c &= \frac{2\pi}{\hbar} \frac{n_i^c}{\mathcal{A}} \left(\frac{e^2}{2\epsilon_0 \kappa (|\mathbf{k} - \mathbf{k}'| + k_{\text{TF}})} \right)^2 |\langle \mathbf{k}' | \mathbf{k} \rangle|^2 \delta(\epsilon_{\mathbf{k}} - \epsilon_{\mathbf{k}'}), \\ w_{\mathbf{k},\mathbf{k}'}^g &= \frac{2\pi}{\hbar} \frac{n_i^g}{\mathcal{A}} V_g^2 e^{-q^2 \sigma^2} \sigma^4 |\langle \mathbf{k}' | \mathbf{k} \rangle|^2 \delta(\epsilon_{\mathbf{k}} - \epsilon_{\mathbf{k}'}),\end{aligned}\quad (10)$$

where \mathcal{A} is the area, $|\mathbf{k}\rangle$ is the energy eigenfunction obtained by diagonalizing Eq. (1), and $\{n_i^\delta, n_i^c, n_i^g\}$ represent the impurity density for different impurity types.

Before proceeding further, we briefly comment on the validity of the Boltzmann approximation assumed throughout this manuscript. The Boltzmann formalism is in general valid if the number of occupied Landau levels is large, i.e., when the magnetic field $b \ll (\epsilon_F - m)^2 / e\hbar v^2$. For a field of $b \sim 0.01T$ and for $(\epsilon_F - m) \sim 4 \text{ meV}$, the ratio $eb\hbar v^2 / (\epsilon_F - m)^2 \sim 0.4$, placing a rough limit on the range of validity of our formalism. For higher values of magnetic fields, the lower limit on ϵ_F increases as well. Nonetheless, we plot the respective quantities over a wide range of the Fermi energy to demonstrate the qualitative trend and the transition from the valence to the conduction bands.

To comment more, in the presence of a magnetic field ($\mathbf{B} = \nabla \times \mathbf{A}$) applied in the z direction, the Hamiltonian of the massive α - T_3 model becomes

$$\begin{aligned}H &= \frac{\sqrt{2}\hbar v}{l_B} \begin{pmatrix} 0 & a \cos \psi & 0 \\ a^\dagger \cos \psi & 0 & a \sin \psi \\ 0 & a^\dagger \sin \psi & 0 \end{pmatrix} \\ &+ m \begin{pmatrix} 1 & 0 & 0 \\ 0 & 0 & 0 \\ 0 & 0 & -1 \end{pmatrix},\end{aligned}\quad (11)$$

where

$$\begin{aligned}a &= \frac{l_B}{2} (\Pi_x - i\Pi_y), \\ a^\dagger &= \frac{l_B}{2} (\Pi_x + i\Pi_y), \\ l_B &= \sqrt{\frac{\hbar}{eB}}, \\ \mathbf{\Pi} &= \mathbf{k} + \frac{e\mathbf{A}}{\hbar}.\end{aligned}\quad (12)$$

Since the evaluation of the energy spectrum at arbitrary values of ψ yields complicated expressions, we can choose a special case of $\psi = \pi/4$. The energy spectrum (in the conduction band) is then given by $\epsilon_n = \sqrt{m^2 + 2eB\hbar v^2 n}$. The difference in energy between two successive Landau levels is given by $\Delta E = e\hbar B v^2 / m$. For the quasiclassical approximation to be valid $\Delta E \ll \epsilon_F - m$. This places a limit on the magnetic field for a fixed value of the chemical potential. Alternatively, we may also say that, for a fixed value of the magnetic field, the theory is valid only when the Fermi energy is above a certain threshold. In Fig. 2, we plot $\Delta E / (\epsilon_F - m)$ as a function of the magnetic field and the Fermi energy for $\psi = \pi/8$. We note

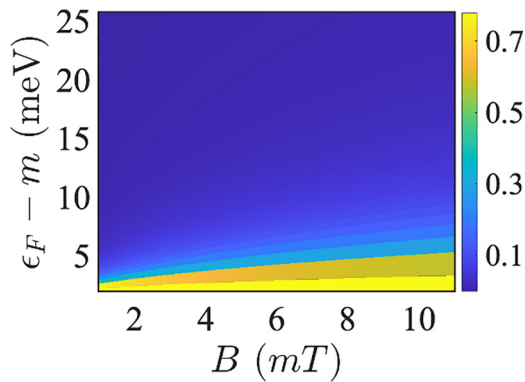


FIG. 2. $\Delta E/(\epsilon_F - m)$ as a function of the Fermi energy and magnetic field for the α - T_3 model. We choose $\psi = \pi/8$.

that, for higher values of the magnetic field, the Fermi energy needs to be larger for the Boltzmann analysis to be valid.

Returning back to magnetotransport, we first discuss the case of massless fermions. Even though the energy spectrum is independent of the parameter ψ , the eigenfunctions are ψ dependent, and therefore one may expect qualitative and/or quantitative differences in the transport behavior. In particular, note that

$$|\langle \mathbf{k}' | \mathbf{k} \rangle|^2 = \frac{1}{4} \cos^2 \left(\frac{\phi - \phi'}{2} \right) [\cos(\phi - \phi') + 3] + \frac{1}{8} \cos(4\psi) \sin^2(\phi - \phi') \quad (13)$$

depends nontrivially on ψ . Thus the scattering rate and conductivity depend crucially on ψ as well. We evaluate the conductivity by numerically calculating conductivity from Eq. (6). In Fig. 3 we plot the conductivity for the massless α - T_3 model. We find that for δ disorder, the longitudinal

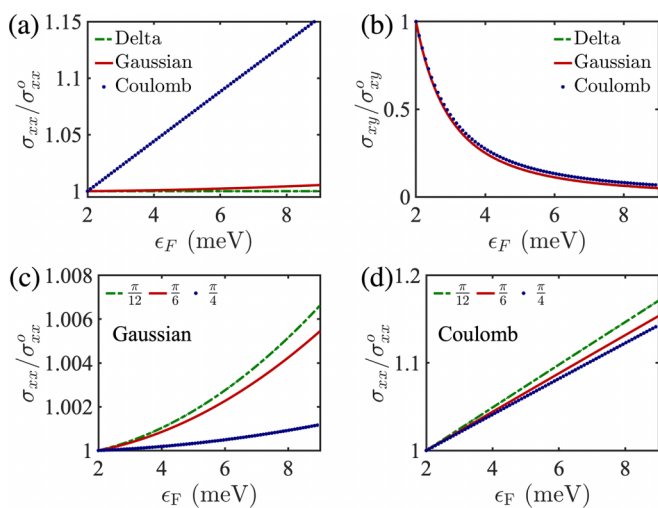


FIG. 3. Conductivity for the α - T_3 model when $m = 0$ and $\psi = \pi/4$. (a) σ_{xx} and (b) σ_{xy} for different disorder types. Comparison of σ_{xx} for different values of ψ is presented in (c) for Gaussian impurities and in (d) for Coulomb impurities. $\sigma_{\alpha\beta}^0$ represent the values of $\sigma_{\alpha\beta}$ at $\epsilon_F = 2$ meV. We chose $k_{TF} = 0.1$ nm, $\sigma = 6$ nm, $b = 0.01T$, $\kappa = 1$, and $V_\delta = V_g = 1$ meV \times (100 nm) 2 .

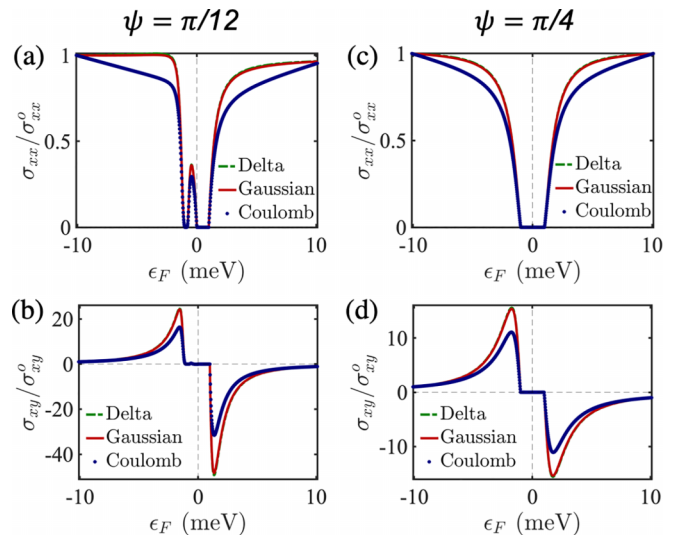


FIG. 4. Conductivity in the case of α - T_3 lattice with a finite mass term. Longitudinal conductivity for (a) $\psi = \pi/12$ and (c) $\psi = \pi/4$. Hall conductivity for (b) $\psi = \pi/12$ and (d) $\psi = \pi/4$. We chose $m = 1$ meV. All other parameters are chosen as in Fig. 3.

conductivity σ_{xx} is independent of the Fermi energy, similar to graphene. This is because for a δ -type disorder, the scattering rate $w_{\mathbf{k}\mathbf{k}'}$ is momentum independent and therefore, on increasing the carrier density, the scattering time $\tau_{\mathbf{k}}$ decreases due to increase in the Fermi surface area. This decrease in the scattering time is exactly compensated by the increase in the density of states, resulting in a density independent conductivity. For Gaussian disorder, the scattering rate ($w_{\mathbf{k}\mathbf{k}'} \sim e^{-|\mathbf{k}-\mathbf{k}'|^2}$) decreases with increasing Fermi surface, and so is the case with Coulomb disorder ($w_{\mathbf{k}\mathbf{k}'} \sim 1/|\mathbf{k}-\mathbf{k}'|^2$). This accounts for the increased conductivity with increase in the Fermi energy, again resembling graphene. On the other hand, the Hall conductivity depends on the curvature of the Fermi surface, which is inversely proportional to the Fermi energy. The Hall conductivity is thus seen to decrease with increasing Fermi energy for all disorder profiles. Furthermore, we also compare the effect of disorder for different values of the parameter ψ . We find that changing ψ quantitatively affects the dependence on the Fermi energy, as shown in Figs. 3(c) and 3(d). Increasing ψ from zero to $\pi/4$ decreases the magnitude of the conductivity.

We next consider the presence of a finite nonzero mass. The band structure, as observed in Fig. 1, acquires a gap between the lower band and the middle band and also between the middle band and the upper band. Furthermore, the electron-hole symmetry is typically violated, except when $\psi = \pi/4$. When $\psi = \pi/4$, the middle band remains dispersionless but is otherwise dispersive for any general value of ψ . Valley symmetry is, however, retained, and hence we focus only near one of the two valleys. In Fig. 4 we plot the longitudinal as well as the Hall conductivity for two values of the parameter ψ . When $\psi = \pi/12$, and if the Fermi energy lies either in the valence or the conduction band, we observe the longitudinal conductivity [Fig. 4(a)] to be almost independent of electron density for Gaussian and δ impurities, indicating the reminiscence of Dirac-like dispersion in the limit $\psi \rightarrow 0$. The small

peak in conductivity when $\epsilon_F < 0$ is due to the dispersive middle band. For Coulomb impurities, we observe a linear dependence on Fermi energy similar to the massless case. When $\psi = \pi/4$, the density dependence is no longer constant for Gaussian and δ impurities, indicating a departure from the Dirac limit [Fig. 4(c)]. The central peak is absent in this case due to the dispersionless middle band. The Hall conductivity peaks (with opposite signs) when the Fermi energy is just above or below the band gap [Fig. 4(b) and Fig. 4(d)]. The electron-hole asymmetry is also reflected in the Hall conductivity in Fig. 4(b).

III. BERRY PHASE EFFECTS IN PSEUDOSPIN-1 FERMIONS

A. Orbital magnetic moment and Berry curvature

Until now, we have neglected the effects of Berry curvature ($\Omega_{\mathbf{k}}$) and the orbital magnetic moment ($\mathbf{m}_{\mathbf{k}}$). In the limit when the mass $m = 0$, both of these quantities vanish exactly. When the mass is nonzero, the orbital magnetic moment, as well as the Berry curvature, are finite and peak at certain points in the Brillouin zone. More generally, the presence of Berry curvature in a system implies breaking either time-reversal (TR) or spatial inversion (SI) symmetry. The Berry curvature is evaluated as

$$\Omega_{\mathbf{k}}^{n\gamma} = i \sum_{n' \neq n} \frac{\langle n | dH/dk^\alpha | n' \rangle \langle n' | dH/dk^\beta | n \rangle - (\alpha \leftrightarrow \beta)}{(\epsilon_{\mathbf{k}}^n - \epsilon_{\mathbf{k}}^{n'})^2}, \quad (14)$$

where n is the band index, α , β , and γ represent the components of the vector, and $|n\rangle$ is the energy eigenket. Simultaneously, the self-rotation of the Bloch wave packet also generates an intrinsic anomalous orbital magnetic moment that is given by [1]

$$\mathbf{m}_{\mathbf{k}}^n = \frac{-ie}{2\hbar} \langle \nabla_{\mathbf{k}} n | \times [H - \epsilon_{\mathbf{k}}^n] | \nabla_{\mathbf{k}} n \rangle. \quad (15)$$

In Fig. 5 we plot the orbital magnetic moment and the Berry curvature for all three bands as a function of the radial momentum k and the lattice parameter ψ . Specifically we plot the z component of $\mathbf{m}_{\mathbf{k}}$ and $\Omega_{\mathbf{k}}$ since the x and y components are zero. As discussed, both the orbital magnetic moment and the Berry curvature acquire finite values in the Brillouin zone. When $\psi \rightarrow 0$, the lower two bands touch each other away from $k = 0$ [Fig. 1(b)], which generates a peak in the Berry curvature and the orbital magnetic moment. In the limit $\psi \rightarrow \pi/2$, the upper two bands touch each other away from $k = 0$, which generates similar peaks as well. This feature is consistent with the fact that the model has a $\alpha \rightarrow 1/\alpha$ duality, i.e., in the limit of $\psi \rightarrow 0$ and $\psi \rightarrow \pi/2$ the model maps onto the graphene lattice. We restrict our discussion to $\tau = +1$ as switching the valley index only reverses the sign of the orbital magnetic moment and the Berry curvature. Importantly, we also note the qualitative differences in the Berry curvature distribution and the orbital magnetic moment between the spin-1/2 Dirac fermions in a gapped graphene model [33] and the pseudospin-1 fermions here. In the model of gapped graphene, these quantities peak exactly at the \mathbf{K} point unlike what we observe in Fig. 5.

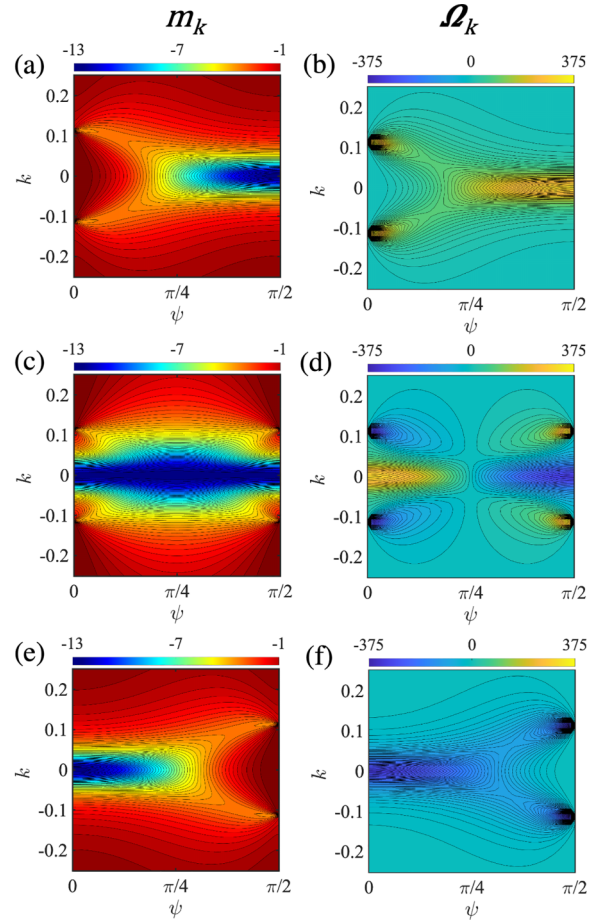


FIG. 5. Orbital magnetic moment $m_{\mathbf{k}}$ for (a) the lower band, (c) the middle band, and (e) the upper band as a function of the radial momentum and the parameter ψ for the α - T_3 lattice model. The corresponding Berry curvature is displayed on the right panels, (b), (d), and (f), respectively. Here, k is in the units of $1/a$, $m_{\mathbf{k}}$ is in the units of ave , and $\Omega_{\mathbf{k}}$ is in the units of $1/a^2$. The mass parameter was chosen $m = 1$ meV and $\tau = +1$.

A nonzero flux of Berry curvature in the Brillouin zone leads to a geometrical contribution to the Hall conductivity, but since here the overall Berry curvature vanishes on adding contributions from both the valleys, the geometrical contribution to the Hall conductivity is zero. However, as we shall shortly see, a small but finite magnetic field results in a finite geometrical Hall conductivity (along with the usual Lorentz-force driven Hall conductivity) due to the breakdown of valley symmetry. More specifically, the anomalous magnetic moment couples to the applied magnetic field as $\epsilon_{\mathbf{k}}^n \rightarrow \epsilon_{\mathbf{k}}^n - \mathbf{m}_{\mathbf{k}}^n \cdot \mathbf{b}$, where \mathbf{b} is the applied magnetic field. Since the sign of the orbital magnetic moment is opposite at both the valleys, the valley symmetry is lost on application of magnetic field. This is highlighted in Fig. 6, which plots the energy dispersion of the α - T_3 model both in the presence and absence of orbital magnetic moment. Interestingly, we find that the energy dispersion not only shifts upwards or downwards depending on the valley, but multiple Fermi surfaces may result depending on the value of the chemical potential due to unequal shifting of various bands. For example, in Figs. 6(a) and 6(b), if the

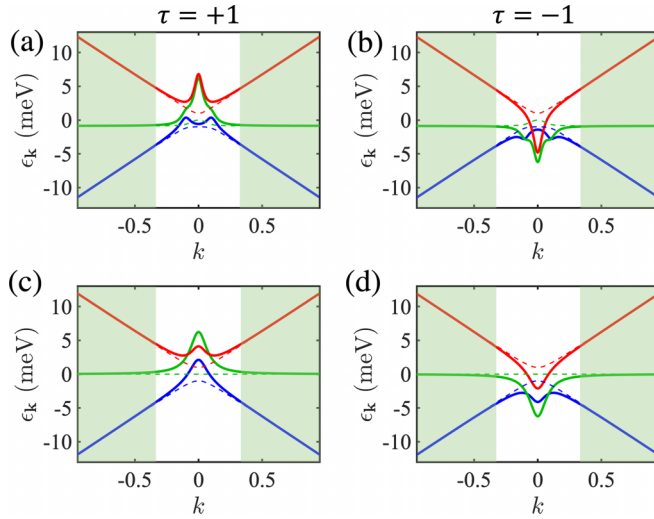


FIG. 6. Band structure of the α - T_3 model considering the effect of coupling to the magnetic field due to a finite anomalous orbital magnetic moment. (a) $\tau = +1$, $\psi = \pi/12$, (b) $\tau = -1$, $\psi = \pi/12$, (c) $\tau = +1$, $\psi = \pi/4$, and (d) $\tau = -1$, $\psi = \pi/4$. The dashed lines represent the dispersion without considering the orbital magnetic moment, i.e., $eb\hbar v^2/(\epsilon_F - m)^2 \gtrsim 0.4$. The shaded region represents the region where quasiclassical analysis is fully valid. We choose $b = 0.01$ T.

Fermi level intersects in the upper band, one may encounter a situation where, on application of a magnetic field, an electronlike Fermi surface additionally acquires one or two holelike Fermi surfaces due to the bending of both the upper band and the middle band. Similarly, if the chemical potential intersects the lower band, then an analogous situation may arise in the other valley [Figs. 6(c) and 6(d)]. Furthermore, an interesting situation is encountered if the chemical potential intersects close by the middle band, where the Fermi surface consists of electron and holelike pockets on the positive and negative valleys, respectively, or vice versa, depending on the direction of the magnetic field. This may result in exact compensation of charges for $\psi = \pi/4$ at a suitable value of the chemical potential [Figs. 6(b) and 6(d)], yielding a compensated semimetal. In Fig. 6 we shade the region where we generally expect the quasiclassical approximation to be valid. Typically, in the vicinity of the level crossings the validity would hold for a lesser value of magnetic field. We next discuss the implications of the effect of orbital magnetic moment and Berry phase on electronic transport.

B. Unconventional transport

In Fig. 7, we plot the longitudinal conductivity for the α - T_3 lattice in the presence of orbital magnetic coupling as a function of the Fermi energy. The behavior of longitudinal conductivity is strikingly different when compared to the case when the orbital magnetic moment is absent. In Fig. 7(a), we observe that the lower band contributes only just below the Fermi energy and the middle band has two large peaks far above and below ϵ_F , each accompanied by two smaller peaks. The upper band has a contribution above and below ϵ_F as well. As expected, the conductivity profile is congruent

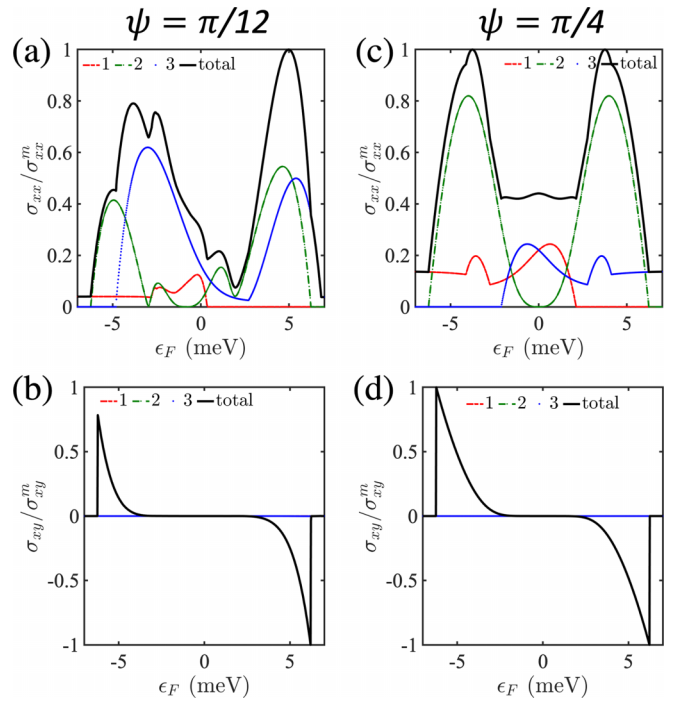


FIG. 7. (a), (c) Longitudinal conductivity as a function of the chemical potential including the effect of orbital magnetic moment. The red, green, and blue curves indicate the contribution from the lower (1), middle (2), and upper (3) bands, respectively. The black curve indicates the net contribution. Here $m = 1$ meV and $b = 0.01$ T. (b), (d) The corresponding Hall conductivity. The dominant contribution is from the middle band. All plots are normalized with respect to their absolute maximum values.

with the band structure presented in Figs. 6(a) and 6(b). The Hall conductivity [Fig. 7(c)], being sensitive to the Fermi surface curvature, has a primary contribution from the middle band that peaks when the band is either close to being fully occupied or fully empty. We find that the Hall contribution from the upper and the lower band are at least one order lesser than the contribution of the middle band. Figure 7(b) and Fig. 7(d) present the longitudinal and Hall conductivity when $\psi = \pi/4$, where electron-hole symmetry is restored in this case. Furthermore, we find that, unlike Fig. 3 and Fig. 4, the qualitative trend is much less sensitive to the nature of the underlying impurities, because the primary deviations on account of the orbital magnetic moment further remove the *Diracness* in the dispersion of the quasiparticles.

The nontrivial Berry curvature of the energy bands guarantees a nonzero charge that is given by

$$c^n = \frac{1}{2\pi} \int d^2\mathbf{k} \Omega_{\mathbf{k}}^n. \quad (16)$$

In Fig. 8(a), we plot the local valley charge for the massive α - T_3 lattice at the $\tau = +1$ valley as a function of the parameter ψ . The presence of nonzero local valley charge gives rise to a geometrical contribution to the Hall conductivity, given by

$$\sigma_{xy}^a = \sum_n \int \frac{d^2\mathbf{k}}{(2\pi)^2} \Omega_{\mathbf{k}}^n f_0^n(\mathbf{k}). \quad (17)$$

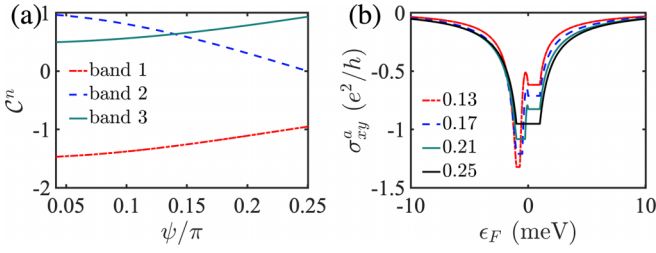


FIG. 8. (a) Valley charge at $\tau = +1$ as a function of the parameter ψ . (b) The geometrical Hall conductivity contribution of $\tau = +1$ as a function of the Fermi energy. We chose $m = 1$ meV. Since C^n at $\tau = -1$ is negative of the value at C^n , the total geometrical Hall conductivity given by the contribution of the two valleys is zero. In plot (b), different curves represent the different values of ψ/π .

The valley charge C^n defined in Eq. (16) integrates the Berry curvature locally around the valley. The integration cutoff is chosen typically corresponding to the energy of 5 meV; however, this is arbitrary and C^n is independent of the cutoff. In Fig. 8(b), we plot the geometrical Hall conductivity contribution of $\tau = +1$ as a function of the Fermi energy. Since C^n at $\tau = -1$ is of the opposite sign of C^n at $\tau = +1$, the total geometrical Hall conductivity given by the contribution of the two valleys is zero.

As noted before, the presence of a magnetic field induces a Zeeman-like contribution to the energy spectrum that is of opposite sign at both valleys; hence the contribution of the geometrical Hall conductivity at both valleys does not cancel out due to their Fermi surfaces being dissimilar as a result of coupling to the magnetic field. This yields a finite geometric Hall conductivity, as plotted in Fig. 9(a), which shows σ_{xy}^a as a function of b for various values of the parameter ψ . In evaluating σ_{xy}^a , we have fixed the Fermi energy so that it intersects only the upper band with a single Fermi surface and thus contributions from the middle and the lower bands are zero. In Fig. 9(b) we plot the ratio of the geometrical Hall conductivity (σ_{xy}^a) to the conventional conductivity (σ_{xy}) for three different values of the disorder potential. While the strength of the disorder potential does not affect the geometric Hall conductivity, it does affect the conventional Hall conductivity. Depending on the strength of the disorder, $\sigma_{xy}^a/\sigma_{xy}$ can be either lesser or greater than one. The ratio, however, is largely independent of the magnetic field since both the

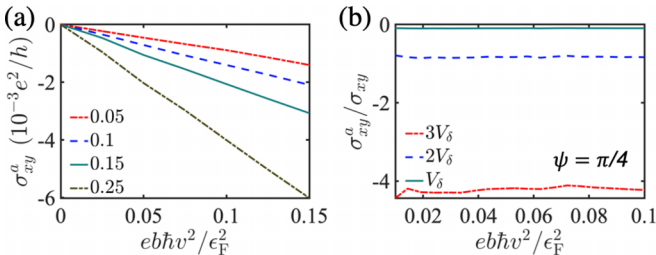


FIG. 9. (a) Total geometrical Hall conductivity σ_{xy}^a as a function of the magnetic field. (b) The ratio of the geometrical (σ_{xy}^a) and the conventional Hall conductivity (σ_{xy}) for three different values of the disorder potential V_δ and fixed $\psi = \pi/4$. In plot (a), different curves represent the different values of ψ/π .

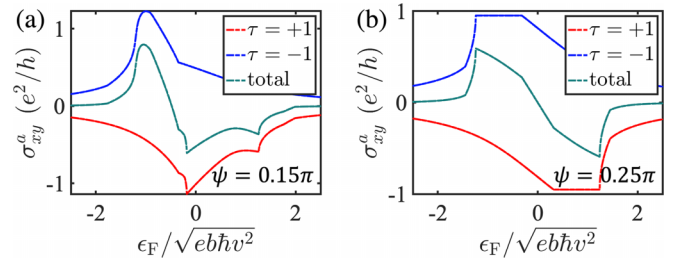


FIG. 10. Total geometrical Hall conductivity σ_{xy}^a as a function of the Fermi energy.

geometrical and the conventional Hall conductivity increase linearly with b . Last, we also highlight another important difference between conventional and geometrical Hall conductivity: Their opposite signs. In Fig. 10 we plot the total geometrical Hall conductivity as a function of the Fermi energy. On comparison to Ref. [29], which calculates σ_{xy} in the ultraquantum limit, we reproduce some qualitative features, such as σ_{xy} becomes large near $\mu = 0$ and flips sign around $\mu = 0$.

C. Magnetoresistance

We now discuss the (longitudinal) magnetoresistance in the $\alpha\mathcal{T}_3$ model. Magnetoresistance from a single parabolic band is ideally zero (but conductivity is typically nonzero). Deviations from parabolicity and/or multiband effects may however yield a finite magnetoresistance. In the present case, the dissimilarity of the Fermi surfaces on account of the magnetic field yields a finite longitudinal magnetoconductivity $\sigma_{xx}(B)$. Depending on how the Hall conductivity varies with the magnetic field (and how much), we anticipate a nontrivial magnetoresistivity in the $\alpha\mathcal{T}_3$ model. Before explicitly evaluating the magnetoresistance in the $\alpha\mathcal{T}_3$ model, we consider a generic toy model for magnetoresistance. The Hall conductivity, whether geometric or conventional, typically has a linear dependence on the magnetic field, while the longitudinal magnetoconductivity is typically quadratic. This motivates us to consider the following conductivity tensor:

$$\hat{\sigma} = \begin{pmatrix} \beta h^2 + \sigma^o & \gamma h + \eta h \\ -\gamma h - \eta h & \beta h^2 + \sigma^o \end{pmatrix}. \quad (18)$$

Here h is the dimensionless magnetic field, the dimensionless longitudinal conductivity at zero magnetic field is σ^o , β is the quadratic coefficient of the longitudinal conductivity, γ is the linear coefficient of the conventional contribution to the Hall conductivity, and η is the linear coefficient of the geometrical contribution to the Hall conductivity. Since both the conventional and the geometric Hall conductivities are typically linear in h , it is possible to do this segregation. The magnetoresistivity $\delta\rho(h)$ is defined as

$$\delta\rho(h) = \frac{\rho_{xx}(h) - \rho_{xx}(0)}{\rho_{xx}(0)}, \quad (19)$$

where $\rho_{xx}(h)$ is the (1,1) component of the resistivity tensor $\hat{\rho} = \hat{\sigma}^{-1}$. In the current model,

$$\delta\rho(h) = \frac{\sigma^o[h^2(\beta) + \sigma^o]}{h^4(\beta)^2 + h^2(\gamma + \eta)^2 + 2h^2\sigma^o(\beta) + (\sigma^o)^2} - 1. \quad (20)$$

We may Taylor expand $\delta\rho(h)$ in powers of magnetic field as

$$\begin{aligned} \delta\rho(h) = & -\frac{[(\gamma + \eta)^2 + \sigma^o(\beta)]}{(\sigma^o)^2}h^2 \\ & + \frac{[(\gamma + \eta)^4 + (\sigma^o)^2(\beta)^2 + 3\sigma^o(\beta)(\gamma + \eta)^2]}{(\sigma^o)^4}h^4 \\ & + O(h^6). \end{aligned} \quad (21)$$

It is possible to analytically calculate the n th power of h in the series expansion of $\delta\rho(h)$, and we find that the coefficients always appear in the numerator, separately in the powers of $(\gamma + \eta)$ and β . However, a second-order expansion is generally sufficient for our purpose, as we are focusing only in the limits of low magnetic fields.

We first analyze the conventional contribution to magnetoresistivity, i.e., we set $\eta = 0$. Clearly, at lower values of magnetic field, the magnetoresistivity is positive if $\beta < -\gamma^2/\sigma^o$; for all other cases the magnetoresistivity is negative. The sign of magnetoresistivity is independent of the sign of γ or, in other words, independent of the type of charge carriers in the system, as expected. In the low-field limit, when the magnetoconductivity is negative and if quadratic coefficient β is negative and below $< -\gamma^2/\sigma^o$, we obtain positive magnetoresistivity. Above a critical value of the magnetic field, $h_c = (\sqrt{-\gamma^2 - \beta\sigma^o})/\beta$, the magnetoresistivity eventually becomes negative. Remarkably, the same analysis works for the geometric contribution as well. To evaluate the geometric contribution, we set $\gamma = 0$. We again find that in the low-field limit, when the magnetoconductivity is negative and if quadratic coefficient β is negative and below $< -\eta^2/\sigma^o$, we obtain positive magnetoresistivity and negative magnetoresistivity otherwise.

For conventional Hall conductivity, the coefficient γ depends on the disorder strength, but coefficient η is independent of disorder for the geometric Hall conductivity. The contribution to the coefficient β mainly arises from the coupling of the anomalous orbital magnetic moment to the magnetic field and is therefore independent of the disorder strength. Note that, in particular, we are focusing on the intrinsic contribution due to the orbital magnetic moment and the extrinsic contribution due to the orbital magnetic moment is likely to be dependent on the disorder. Finally, σ^o clearly depends on the strength of the disorder. It is thus likely that the magnetoresistivity contribution from the conventional Hall effect or the geometrical Hall effect can be either positive or negative due to competing effects of β (independent of disorder) and γ (dependent on disorder), and σ^o (dependent on disorder). Although, our model is applicable to the system considered in Ref. [10] (gapped graphene), a discussion on the possibility of both signs of magnetoresistance remains absent in their work. We conjecture that, as a result of orbital magnetic moment coupling, both positive and negative magnetoresis-

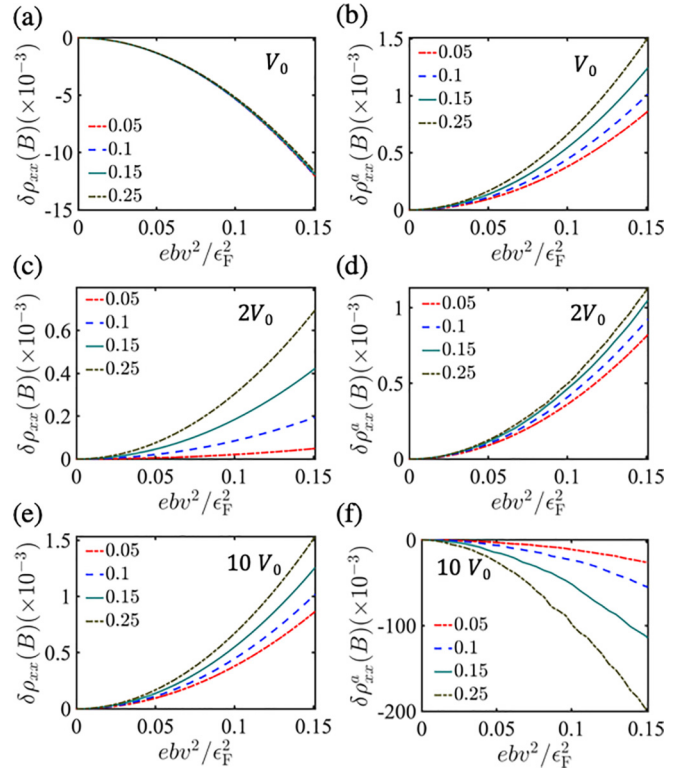


FIG. 11. Magnetoresistivity in the α - \mathcal{T}_3 model for various values of the parameter ψ . Panels (a), (c), and (e) plot the contribution due to conventional Hall effect, for different disorder strengths; (b), (d), and (f) plot the contribution due to geometrical Hall effect. We use Dirac type impurities here and $V_0 = 1 \text{ meV} \times (100 \text{ nm})^2$.

tance should be observed in gapped graphene (Ref. [10]) as well.

In Fig. 11 we plot the magnetoresistivity for the α - \mathcal{T}_3 model, separately for the conventional and the geometrical Hall contributions, thus revealing their qualitative differences. As the strength of disorder is increased, we observe that the conventional contribution to magnetoresistivity switches sign from negative to positive, and decreases in the overall magnitude, because on increasing the disorder strength, the condition $\beta < -\gamma^2/\sigma^o$ is satisfied much more easily. Even though $1/\sigma^o$ increases on increasing disorder, γ^2 decreases even more rapidly, thus making the requirement for β to be lesser than $-\gamma^2/\sigma^o$ easier to be realized, yielding positive magnetoresistivity. Contrary to this, we find that, on increasing disorder, the geometrical contribution to the magnetoresistivity changes sign from positive to negative. This is because $1/\sigma^o$ increases on increasing disorder, but η^2 remains constant, therefore making it harder to realize the condition $\beta < -\eta^2/\sigma^o$ for positive magnetoresistivity. Furthermore, the magnitude of magnetoresistivity increases as well, because the magnitude of the geometrical Hall conductivity remains a constant, while that of σ^o decreases. We close this section with the remark that the geometrical electronic transport quantities will also reflect on the geometrical thermoelectric quantities. For instance, the derivative of the Hall conductivity with respect to the Fermi energy yields the Nernst effect, which should also be substantially measurable here. We defer the

evaluation of geometrical thermoelectric coefficients in the α - \mathcal{T}_3 model to future works.

IV. CONCLUSIONS

While the α - \mathcal{T}_3 model of pseudospin-1 fermions owes similarities to the model of pseudospin-1/2 Dirac fermions, the effects on electronic transport are more nuanced. Even though their energy dispersion is qualitatively similar, presence of the middle band in the α - \mathcal{T}_3 lattice changes the wave functions' topology and, more so, the distribution of the Berry curvature and the orbital magnetic moment in the Brillouin zone. Here we studied electronic transport in the α - \mathcal{T}_3 model and evaluate their conventional as well as the geometrical transport responses in the presence of weak electric and magnetic fields. First, we listed out the differences arising in the conventional conductivity (longitudinal and Hall) for three different types of impurities: δ -correlated disorder, Gaussian disorder, and Coulomb disorder. Second, we studied the Berry curvature and orbital magnetic moment of the pseudospin-1 fermions and evaluate their geometrical transport responses. An important finding

of this work is that coupling the orbital magnetic moment to the external magnetic field breaks valley symmetry, results in finite and measurable corrections to the conductivity, and yields a nontrivial geometrical Hall conductivity due to the nonzero distribution of the flux of the Berry curvature. Third, we found that a finite longitudinal magnetoresistance is induced by the orbital magnetic moment, which can be of either sign: Positive or negative, depending on the amount of disorder, a feature which can be contrasted to pseudospin-1/2 fermions discussed in Ref. [10]. Recent material advances and upcoming experiments on $\text{Hg}_{1-x}\text{Cd}_x\text{Te}$ quantum wells, trilayers of cubic lattices that may realize pseudospin-1 fermions, makes our study even more appropriate.

ACKNOWLEDGMENTS

A.S. acknowledges support from IIT Mandi HTRA. G.S. acknowledges support from SERB Grant No. SRG/2020/000134 and the IIT Mandi Seed Grant No. IITM/SG/GS/73.

-
- [1] D. Xiao, M.-C. Chang, and Q. Niu, Berry phase effects on electronic properties, *Rev. Mod. Phys.* **82**, 1959 (2010).
- [2] G. Sundaram and Q. Niu, Wave-packet dynamics in slowly perturbed crystals: Gradient corrections and Berry-phase effects, *Phys. Rev. B* **59**, 14915 (1999).
- [3] M.-C. Chang and Q. Niu, Berry Phase, Hyperorbits, and the Hofstadter Spectrum, *Phys. Rev. Lett.* **75**, 1348 (1995).
- [4] M.-C. Chang and Q. Niu, Berry phase, hyperorbits, and the Hofstadter spectrum: Semiclassical dynamics in magnetic Bloch bands, *Phys. Rev. B* **53**, 7010 (1996).
- [5] M.-C. Chang and Q. Niu, Berry curvature, orbital moment, and effective quantum theory of electrons in electromagnetic fields, *J. Phys.: Condens. Matter* **20**, 193202 (2008).
- [6] N. Nagaosa, J. Sinova, S. Onoda, A. H. MacDonald, and N. P. Ong, Anomalous Hall effect, *Rev. Mod. Phys.* **82**, 1539 (2010).
- [7] D. T. Son and B. Z. Spivak, Chiral anomaly and classical negative magnetoresistance of Weyl metals, *Phys. Rev. B* **88**, 104412 (2013).
- [8] J. Ma and D. A. Pesin, Chiral magnetic effect and natural optical activity in metals with or without Weyl points, *Phys. Rev. B* **92**, 235205 (2015).
- [9] D. Varjas, A. G. Grushin, R. Ilan, and J. E. Moore, Dynamical Piezoelectric and Magnetopiezoelectric Effects in Polar Metals from Berry Phases and Orbital Moments, *Phys. Rev. Lett.* **117**, 257601 (2016).
- [10] H. Zhou, C. Xiao, and Q. Niu, Valley-contrasting orbital magnetic moment induced negative magnetoresistance, *Phys. Rev. B* **100**, 041406(R) (2019).
- [11] A. Knoll, C. Timm, and T. Meng, Negative longitudinal magnetoconductance at weak fields in Weyl semimetals, *Phys. Rev. B* **101**, 201402(R) (2020).
- [12] G. Sharma, S. Nandy, and S. Tewari, Sign of longitudinal magnetoconductivity and the planar Hall effect in Weyl semimetals, *Phys. Rev. B* **102**, 205107 (2020).
- [13] K. Das and A. Agarwal, Intrinsic Hall conductivities induced by the orbital magnetic moment, *Phys. Rev. B* **103**, 125432 (2021).
- [14] A. H. Castro Neto, F. Guinea, N. M. R. Peres, K. S. Novoselov, and A. K. Geim, The electronic properties of graphene, *Rev. Mod. Phys.* **81**, 109 (2009).
- [15] S. Das Sarma, S. Adam, E. H. Hwang, and E. Rossi, Electronic transport in two-dimensional graphene, *Rev. Mod. Phys.* **83**, 407 (2011).
- [16] N. P. Armitage, E. J. Mele, and A. Vishwanath, Weyl and Dirac semimetals in three-dimensional solids, *Rev. Mod. Phys.* **90**, 015001 (2018).
- [17] Y. Cao, V. Fatemi, S. Fang, K. Watanabe, T. Taniguchi, E. Kaxiras, and P. Jarillo-Herrero, Unconventional superconductivity in magic-angle graphene superlattices, *Nature (London)* **556**, 43 (2018).
- [18] A. Raoux, M. Morigi, J.-N. Fuchs, F. Piéchon, and G. Montambaux, From Dia- to Paramagnetic Orbital Susceptibility of Massless Fermions, *Phys. Rev. Lett.* **112**, 026402 (2014).
- [19] F. Wang and Y. Ran, Nearly flat band with Chern number $c = 2$ on the dice lattice, *Phys. Rev. B* **84**, 241103(R) (2011).
- [20] J. D. Malcolm and E. J. Nicol, Magneto-optics of massless Kane fermions: Role of the flat band and unusual Berry phase, *Phys. Rev. B* **92**, 035118 (2015).
- [21] E. Serret, P. Butaud, and B. Pannetier, Vortex correlations in a fully frustrated two-dimensional superconducting network, *Europhys. Lett.* **59**, 225 (2002).
- [22] B. Dey and T. K. Ghosh, Photoinduced valley and electron-hole symmetry breaking in α - \mathcal{T}_3 lattice: The role of a variable Berry phase, *Phys. Rev. B* **98**, 075422 (2018).
- [23] T. Bilitewski and R. Moessner, Disordered flat bands on the kagome lattice, *Phys. Rev. B* **98**, 235109 (2018).
- [24] D. Oriekhov, E. Gorbar, and V. Gusynin, Electronic states of pseudospin-1 fermions in dice lattice ribbon, *Low Temp. Phys.* **44**, 1313 (2018).

- [25] SK Firoz Islam and P. Dutta, Valley-polarized magnetoconductivity and particle-hole symmetry breaking in a periodically modulated α - T_3 lattice, *Phys. Rev. B* **96**, 045418 (2017).
- [26] E. Illes, J. P. Carbotte, and E. J. Nicol, Hall quantization and optical conductivity evolution with variable Berry phase in the α - T_3 model, *Phys. Rev. B* **92**, 245410 (2015).
- [27] Á. D. Kovács, G. Dávid, B. Dóra, and J. Cserti, Frequency-dependent magneto-optical conductivity in the generalized α - T_3 model, *Phys. Rev. B* **95**, 035414 (2017).
- [28] T. Biswas and T. K. Ghosh, Magnetotransport properties of the α - T_3 model, *J. Phys.: Condens. Matter* **28**, 495302 (2016).
- [29] Y. Xu and L.-M. Duan, Unconventional quantum Hall effects in two-dimensional massive spin-1 fermion systems, *Phys. Rev. B* **96**, 155301 (2017).
- [30] E. Illes and E. J. Nicol, Magnetic properties of the α - T_3 model: Magneto-optical conductivity and the Hofstadter butterfly, *Phys. Rev. B* **94**, 125435 (2016).
- [31] L. Tamang, T. Nag, and T. Biswas, Floquet engineering of low-energy dispersions and dynamical localization in a periodically kicked three-band system, *Phys. Rev. B* **104**, 174308 (2021).
- [32] L. Tamang and T. Biswas, Probing topological signatures in an optically driven α - T_3 lattice, *Phys. Rev. B* **107**, 085408 (2023).
- [33] D. Xiao, W. Yao, and Q. Niu, Valley-Contrasting Physics in Graphene: Magnetic Moment and Topological Transport, *Phys. Rev. Lett.* **99**, 236809 (2007).
- [34] E. V. Gorbar, V. P. Gusynin, and D. O. Oriekhov, Electron states for gapped pseudospin-1 fermions in the field of a charged impurity, *Phys. Rev. B* **99**, 155124 (2019).
- [35] J. Romhányi, K. Penc, and R. Ganesh, Hall effect of triplons in a dimerized quantum magnet, *Nat. Commun.* **6**, 6805 (2015).
- [36] X. Ye, S.-S. Ke, X.-W. Du, Y. Guo, and H.-F. Lü, Quantum tunneling in the α - t_3 model with an effective mass term, *J. Low Temp. Phys.* **199**, 1332 (2020).
- [37] V. A. Mukhanov, A. Courac, and V. L. Solozhenko, The effect of doping on the lattice parameter and properties of cubic boron nitride, *J. Superhard Mater.* **42**, 377 (2020).
- [38] H. Bruus and K. Flensberg, *Many-Body Quantum Theory in Condensed Matter Physics: An Introduction* (Oxford University Press, Oxford, 2004).